AGU PUBLICATIONS

Geochemistry, Geophysics, Geosystems

RESEARCH ARTICLE
10.1002/2014GC005560

# Segmentation and eruptive activity along the East Pacific Rise at 16°N, in relation with the nearby Mathematician hotspot

**M. Le Saout[1], A. Deschamps[1], S. A. Soule[2], and P. Gente[1]**

[1]Université de Brest, UMR 6538 Domaines Océaniques, Institut universitaire Européen de la Mer, Plouzané, France, [2]Department of Geology and Geophysics, Woods Hole Oceanographic Institution, Woods Hole, Massachusetts, USA

**Key Points:**
- EPR fine-scale segmentation revealed by high-resolution bathymetry
- The Axial Summit Trough geometry reflects variations of the eruptive activity
- The Mathematician hotspot strongly influences the spreading processes at 16°N

**Correspondence to:**
A. Deschamps,
Anne.Deschamps@univ-brest.fr

**Citation:**
Le Saout, M., A. Deschamps, S. A. Soule, and P. Gente (2014), Segmentation and eruptive activity along the East Pacific Rise at 16°N, in relation with the nearby Mathematician hotspot, *Geochem. Geophys. Geosyst.*, *15*, 4380–4399, doi:10.1002/2014GC005560.

Received 27 AUG 2014
Accepted 16 OCT 2014
Accepted article online 21 OCT 2014
Published online 26 NOV 2014

**Abstract** The 16°N segment of the East Pacific Rise is the most overinflated and shallowest of this fast-spreading ridge, in relation with an important magma flux due to the proximity of the Mathematician hotspot. Here, we analyze the detailed morphology of the axial dome and of the Axial Summit Trough (AST), the lava morphology, and the geometry of fissures and faults, in regard to the attributes of the magma chamber beneath and of the nearby hotspot. The data used are 1 m resolution bathymetry combined with seafloor photos and videos. At the dome summit, the AST is highly segmented by 10 third-order and fourth-order discontinuities over a distance of 30 km. Often, two contiguous and synchronous ASTs coexist. Such a configuration implies a wide (1100 m minimum) zone of diking. The existence of contiguous ASTs, their mobility, their general en echelon arrangement accommodating the bow shape of the axial dome toward the hotspot, plus the existence of a second magma lens under the western half of the summit plateau, clearly reflect the influence of the hotspot on the organization of the spreading system. The different ASTs exhibit contrasted widths and depths. We suggest that narrow ASTs reflect an intense volcanic activity that produces eruptions covering the tectonic features and partially filling the ASTs. AST widening and deepening would indicate a decrease in volcanic activity but with continued dike intrusions at the origin of abundant sets of fissures and faults that are not masked by volcanic deposits.

## 1. Introduction

Many mid-ocean ridge segments are under the influence of a hotspot [e.g., *Hey*, 1977; *Mammerickx and Sandwell*, 1986; *Maia et al*., 2000; *Sinton et al*., 2003; *Ito et al*., 2003; *Mittelstaedt et al*., 2008, 2011]. Where ridge-hotspot interactions take place, the spreading axis displays a variety of anomalies including negative Bouguer gravity anomalies related to crustal overthickening or elevated mantle temperatures, enrichment in trace elements and isotopic ratios indicative of deep sources, depth anomalies, off-axis volcanism, and successive axis jumps leading to globally asymmetric accretion and unique seafloor morphologies. While many studies have examined the large-scale, regional expressions of ridge-hotspot interactions, few studies have examined the detailed expressions of this process at the ridge axis. This study uses high-resolution bathymetric and imagery data to document the interaction between the fast-spreading East Pacific Rise (EPR) and a hotspot.

Here, we focus on the detailed morphology of the 16°N segment of the EPR, located 20 km to the east of the Mathematician hotspot, which is reflected by the presence of the Mudskipper volcanic seamount chain (also named "P1545 ridge") [e.g., *Macdonald et al*., 1992; *Weiland and Macdonald*, 1996; *Carlut et al*., 2004]. The seamount chains ends at 15°42'N–105°30'W, i.e., less than 5 km from the western flank of the axial rise. Earlier studies have evidenced the influence of the Mathematician hotspot on the spreading processes at the 16°N segment. As an example, relics of extinct spreading axes to the east of the segment indicate that it has experienced at least two westward jumps in the direction of the hotspot [*Carbotte et al*., 2000; *Shah and Buck*, 2006]. The gravity data show the presence a relatively negative circular Bouguer anomaly, centered on 15°42'N/105°25'W indicating a crustal overthickening of about 2 km in this region [*Weiland and Macdonald*, 1996]. Consistently, this is the most inflated segment of the EPR, suggesting an anomalously large magma input. However, seismic reflection data showed that layer 2A (commonly attributed to the layer of extrusive basalts) has a relatively constant thickness on axis (170 m on average) [*Carbotte et al*., 2000]. Based on this observation, *Shah and Buck* [2006] suggest that the negative gravity anomaly is instead

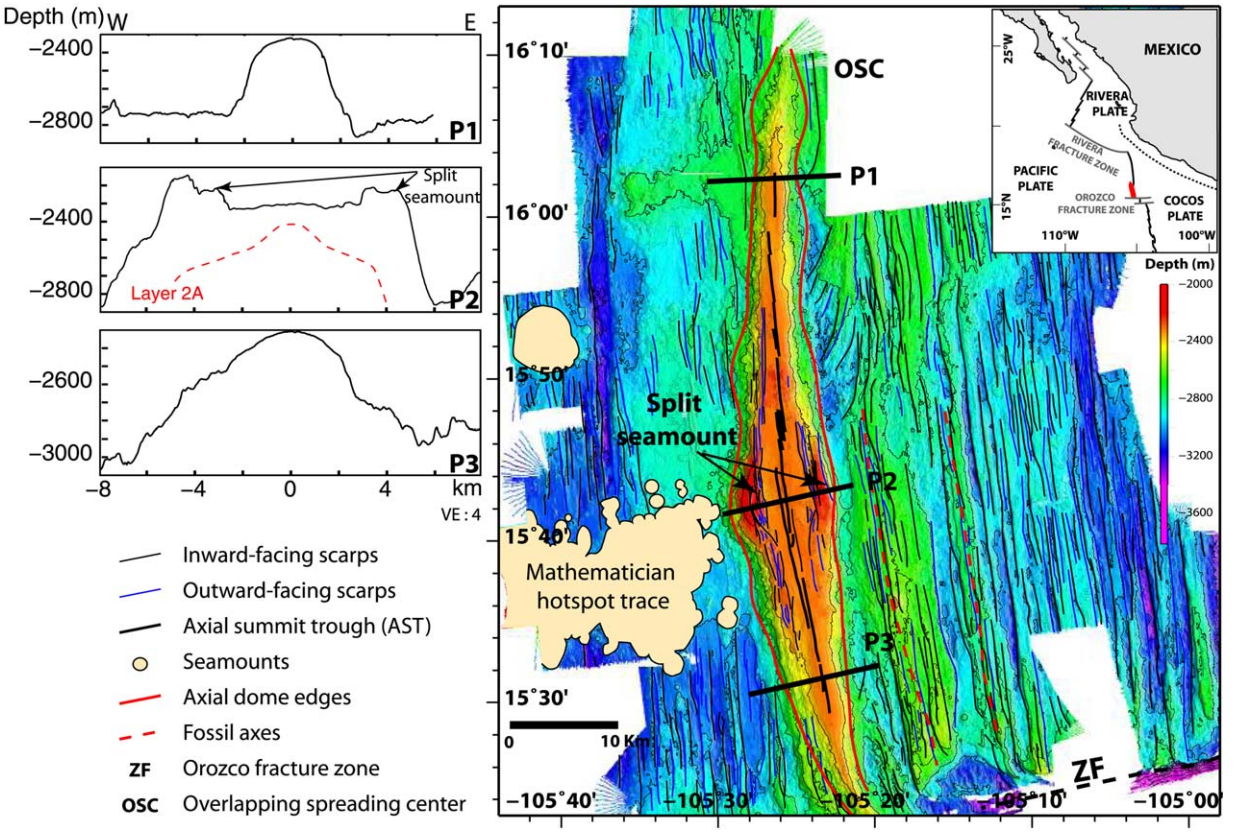


**Figure 1.** Bathymetry of the 16°N segment of the East Pacific Rise, with the main seafloor reliefs. Bathymetric data are gridded with 40 m cells. The location of the study area is indicated in insert. The eastern and western edges of the axial dome (in red), defined at the point of rupture between the relief of the dome and the adjacent abyssal plains are determined based on 178 cross-axis bathymetric profiles, spaced 500 m apart (ex. P1, P2, P3). The profiles P1, P2, and P3 highlight along-axis variations in the axial dome morphology. The base of the seismic layer 2A (extrusive basalts layer) [*Carbotte et al*., 2000] is shown on P2 profile (in red).

related to a zone of high temperature and enhanced melting beneath the ridge axis, due to interaction between the hotspot and the ridge. Moreover, an unusual geochemical signature has also been detected in axial lava near 15°42′N (where the seamount chain meets the ridge). It is characterized by very unradiogenic Pb associated with enriched Sr, Nd, and Hf isotopic compositions, which is interpreted as being one of the geochemical expression of the hotspot [*Mougel et al*., 2014].

In 2010, the PARISUB (PAnache RIdge SUBmersible) oceanographic cruise collected hull-mounted multibeam bathymetry using the R/V L'Atalante and high-resolution, near-bottom bathymetry using the Autonomous Underwater Vehicle (AUV) Aster-X (Ifremer) as well as seafloor photos and videos using the manned submersible Nautile (Ifremer). We use these data to perform a detailed morphological analysis of the eruptive and tectonic processes along the segment, i.e., the geometry and segmentation of the axial summit trough, the morphology and the distribution of the lava flows, and the distribution of tectonic structures, in relation to the deep structure of the ridge (e.g., melt accumulation). The objective was to analyze the relationship between the hotspot and the small-scale segmentation of the axis (third and fourth-order segments) as well as eruptive processes, so as to understand the fine-scale ($<$ 1 km) effects of the ridge-hotspot interaction.

## 2. Geological Context

### 2.1. Overall Morphology

The 16°N segment of the East Pacific Rise is located to the north of the Orozco fracture zone, between 15°25′N and 16°20′N (Figure 1). The full spreading rate is ∼85 mm/yr [*Carbotte et al*., 1998]. This 115 km long segment terminates in the north at an Overlapping Spreading Center (OSC). This zone of overlap stretches over 12 km along the axis [e.g., *Sloan*, 1991; *Macdonald et al*., 1992; *Carbotte et al*., 2000], the two

ridge crests being separated by ~15 km. The shallowest point, at −2200 m, occurs near the projected intersection of the Mudskipper volcanic chain and the ridge axis (15°42′N). This depth is ~400 m shallower than any other segment of the EPR [e.g., *Scheirer and Macdonald*, 1993; *Cormier et al*., 1995; *Wang et al*., 1996; *Carbotte et al*., 2000]. The 16°N segment is also the broadest segment of the EPR (up to 15 km wide). This unusual morphology is attributed to an important magma input related to the proximity of the Mathematician hotspot [e.g., *Scheirer and Macdonald*, 1995; *Weiland and Macdonald*, 1996; *Carbotte et al*., 2000]. The hotspot is inferred to be located about 20 km west of the ridge axis, the Mudskipper volcanic chain being attributed to enhanced volcanism above this hotspot. The hotspot is believed to have caused two axis jumps of 7 and 9 km toward the west at 150 and 300 ka. These jumps would have led to a rapid northwestward migration of the segment (~240 mm/yr) [*Carbotte et al*., 2000; *Shah and Buck*, 2006]. According to *Carbotte et al*. [2000], the segment became established in its present position 85–105 ka ago, which corresponds to the isochron located at the edge between the axial rise and oblique abyssal hills to the east.

Previous analysis of bathymetric, magnetic, and side scan sonar data by *Macdonald et al*. [1992] indicate that the segment has been propagating toward the north at decreasing rates for at least 0.6 Ma: between 0.6 and 0.4 Ma, this extension took place at a rate of 105 mm/yr, then from 0.4 to 0.2 at a rate of 50 mm/yr. The present estimated rate of propagation is ~10 mm/yr.

### 2.2. Segmentation and Structure of the 16°N Segment

Previous cruises have documented the segmentation of the spreading axis between 15°25′N and 16°20′N. Based on data from the SeaMarc II side scan sonar, *Macdonald et al*. [1992] identified three discontinuities in the segment morphology, at 15°43′N, 15°50′N, and 15°58′N. These discontinuities are lateral shifts (or "devals") 1–3 km in amplitude in the axial summit trough (AST). They are defined as "third-order discontinuities" according to the classification of *Macdonald et al*. [1988]. Based on the same data set, *Carbotte et al*. [2000] identified seven discontinuities corresponding to devals and variations in the width of the summit trough: three at 15°38′N, 15°45′N, 15°48′N, respectively, three between 15°53′N-15°55′N and one at 15°59′N. North of 15°38′N the summit trough broadens significantly. At 15°45′N and at 15°48′N, the axis shifts toward the east. Between 15°53′N and 15°55′N, it shifts via three successive OSCs. Finally, north of 15°59′N, it shifts by more than 1 km to the east.

The magma lens marking the roof of the Axial Magma Chamber (AMC), identified using seismic reflection data, is located at a depth of 1300–1500 m under the ridge crest [*Carbotte et al*., 2000]. The across-axis depth variation of the magma lens is relatively limited, being shallower (by 100 m at maximum) directly beneath the AST. Along-axis, the lens is shallowest near 15°35′N and 15°52′N (about 1300 m under the seafloor). It deepens slightly at the center of the segment (near 15°45′N) where it reaches a depth of 1500 m. The lens is 1330 ± 340 m wide, with a maximum width beneath the widest part of the axial dome near 15°43′N [*Carbotte et al*., 2000]. These authors note that under this segment the lens is larger than usually observed elsewhere on the EPR (~500 m at 13°N, ~800 m at 17°S and ~1200 m at 9°N, for example), although still within the previously reported ranges (< 500–4500 m) [e.g., *Detrick et al*., 1987; *Kent et al*., 1990, 1993, 1994]. The lens is observed along almost the whole length of the segment from 15°29′N to 16°02′N, but a few discontinuities can nonetheless be noted:

1. The lens disappears totally under the volcanic edifice located at 15°50′N, probably because of signal disruption due to the roughness of the seafloor in this area.
2. Between 15°58′N and 16°01′N, its disappearance is not attributed to the topography. *Carbotte et al*. [2000] suggest that it could be linked to the 1 km deval of the AST at this location.
3. The lens is poorly marked (i.e., weak reflector) or even interrupted from 15°51′N to 15°57′N and from 15°35′N to 15°38′N, where discontinuities in the AST are observed in the sonar data (see below).
4. The reflector shifts vertically by a 100 m at 15°45′N, being shallower north of this latitude.

It is worth noting that several seismic profiles perpendicular to the ridge axis reveal a second, weaker, reflector, indicating a second magma lens that is nearly continuous between 15°41.5′N and 15°45′N, and located approximately 1.2 km to the west and ~300 m deeper with respect to the magma lens directly below the ASTs.

Layer 2A has a relatively constant thickness of 107 ± 45 m over a region ~750 m wide under the subhorizontal summit plateau. When two magma lenses are observed, the region where the thickness of layer 2A is constant

is centered on the most superficial lens. In both cases, the thickness of layer 2A increases rapidly away of the AST (over a distance of 100–300 m), reaching a thickness of about 350 m under the rest of the summit plateau (which reaches 5 km in width at its broadest point), then about 550–750 m under the high reliefs that mark its edges (Figure 1, profile P2). The thickness of layer 2A under these marginal highs is greater in the east (up to 750 m) than in the west (500 m maximum), and reaches its maximum thickness between 15°40′N and 15°47′N. *Carbotte et al*. [2000] also noted local increases in layer 2A thickness beneath the seamounts of the Mudskipper volcanic chain. Layer 2A also thickens towards the extremities of segment 16°N, and locally, by about 30 m, at 15°50′N, below the 80 m high, prominent volcanic edifice centered on the AST at this latitude.

## 3. Data

Surface bathymetric data were collected using the R/V L'Atalante SIMRAD EM122 hull-mounted multibeam echosounder. They cover a region of about 5700 $km^2$ with a grid size of 40 m. (Figure 1). Over the axial summit plateau, the data were collected by narrowing the beams of the echosounder and reducing the ship speed (5 knots), to produce a bathymetric grid with 10 m cells.

Higher-resolution bathymetric data were collected using a SIMRAD 2000 multibeam echosounder (CNRS/Géosciences Azur) mounted on the AUV Aster-X. These data cover an area of about 120 $km^2$ (4 km across-axis by 30 km along-axis) between 15°36′N and 15°53′N, and 105°24′W and 105°27.5′W on the central part of the summit plateau (Figures 1 and 2). The AUV was operated 70 m above the bottom, along 200 m spaced lines, for a total of 72 km travelled in 110 h. These data allowed us to construct a bathymetric grid with a 1 m spacing.

These data were complemented by a set of photographs and videos taken during dives of the manned submersible Nautile (Ifremer). During the PARISUB cruise, 24 Nautile dives were carried out. Twelve of these dives were led in the zone covered by the high-resolution bathymetric data and provide groundtruthing for interpreting the bathymetric data (Figure 2).

## 4. Observations

### 4.1. Morphology of the 16°N Spreading Segment

In order to study in detail the morphology of the16°N segment, we have analyzed 16 km long bathymetric profiles, spaced 500 m apart, and perpendicular to the ridge axis, using ship-based 40 m cells bathymetry. On these profiles, we identified the eastern and western edges of the axial dome based on the abrupt change in slope where the dome meets the adjacent abyssal plains. The height and width of the dome were measured based on these recordings along the entire length of the segment (i.e., 115 km; Figures 1 and 3). Its width varies from 15 km at its broadest part (near 15°42′N) to 3.1 km in the south and 1.7 km in the north at the edge of the bathymetric data coverage (Figure 3c). Its height varies from 145 to 780 m above the abyssal plains (Figure 3d). The shallowest point of the axial dome (−2200 m) is observed between 15°48′N and 15°51′N, where there is a prominent volcanic edifice. The dome deepens toward the north and the south to depths of at least −2550 m (at 16°10′N; Figure 3b).

We also measured the latitudinal variations of the trend of the axial rise, every 500 m (Figure 3a). Its overall orientation varies by about 33° (from N150°E to N3°E) from one extremity (in the south) to the other (in the north) (Figure 3a). As a result, the segment has a bow shape, the arc being concave East. It should be noted that elsewhere along the EPR, the spreading segments are generally linear and only bend toward their extremities, or over distances of a few tens of kilometres where they overlap with another segment or near transform zones [e.g., *Macdonald et al*., 1984; *Sempere and Macdonald*, 1986]. Therefore, the OSC in the north, and the Orozco fracture zone in the south of the segment, are likely not at the origin of the curved shape of the 16°N segment over a distance of nearly 115 km.

Based on its morphology (height, width, and cross-sectional shape), the axial dome can be divided into three domains: a southern domain (located between the Orozco fracture zone and 15°35.5′N), a central domain (between 15°35.5′N and 15°53.5′N), and a northern domain (between 15°53.5′N and the OSC that marks the northern end of the segment) (Figures 1 and 3):

1. The northern and southern domains display similar morphologies: in section, the axial dome has an upside-down "U" shape (Figure 1, profiles P1 and P3) and culminates at 400 m above the adjacent abyssal

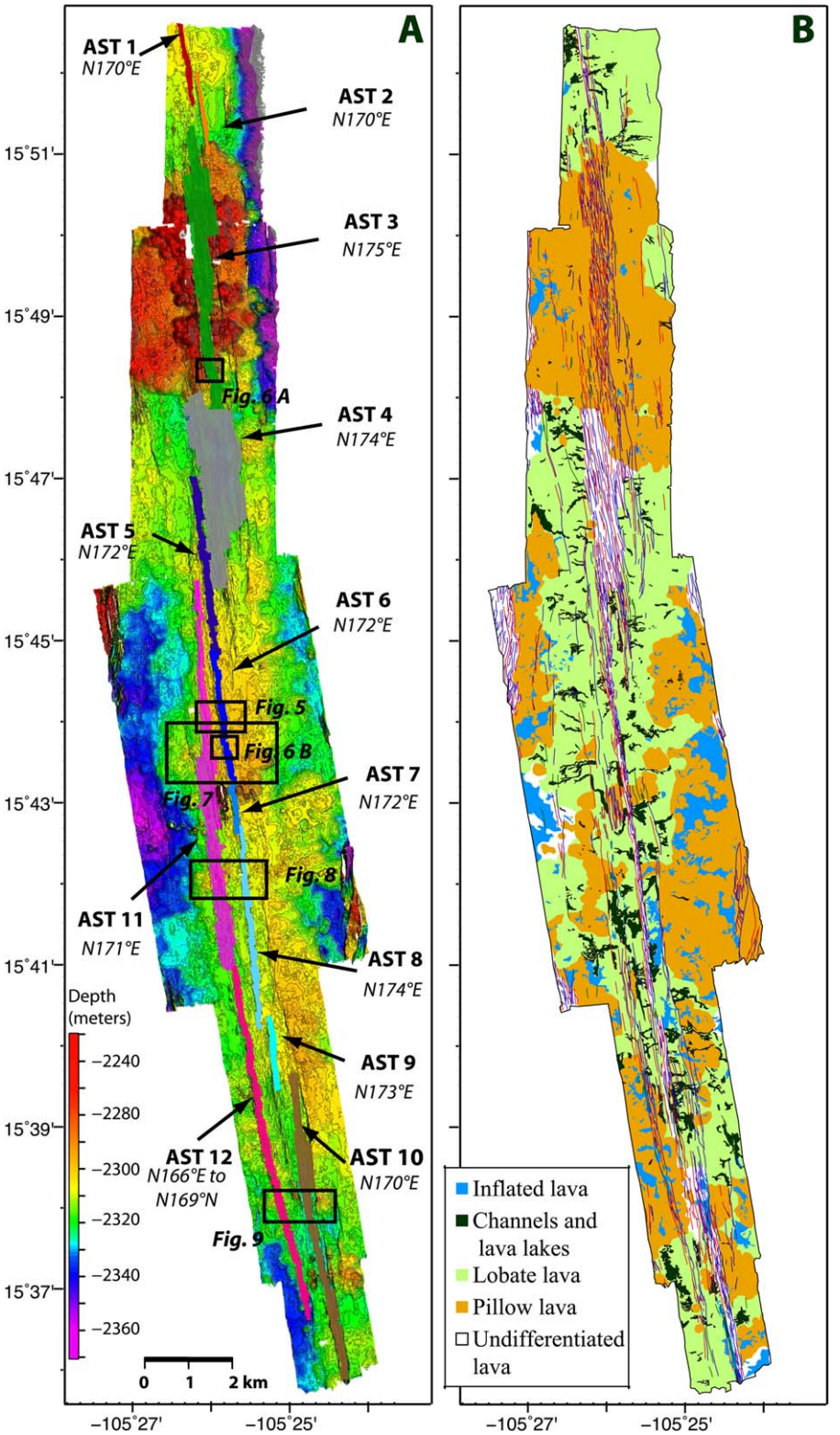


**Figure 2.** (a) High-resolution bathymetric map (1 m grid cell size) of the 16°N segment (East Pacific Rise) acquired using the echosounder Simrad EM2000 mounted on the Aster-X Autonomous Underwater Vehicle (Ifremer). Contour interval is 2 m. Axial Summit Troughs (AST) are named AST 1–AST 12. Their orientations are reported. Black boxes indicate the location of figures 3, 5, 6, and 7. (b) Geological map established based on the joint analysis of video data and high-resolution bathymetry, indicating the distinct volcanic facies and tectonic features (faults and fissures). Westward-facing faults are indicated in blue, eastward ones in red, and fissures in dark green.

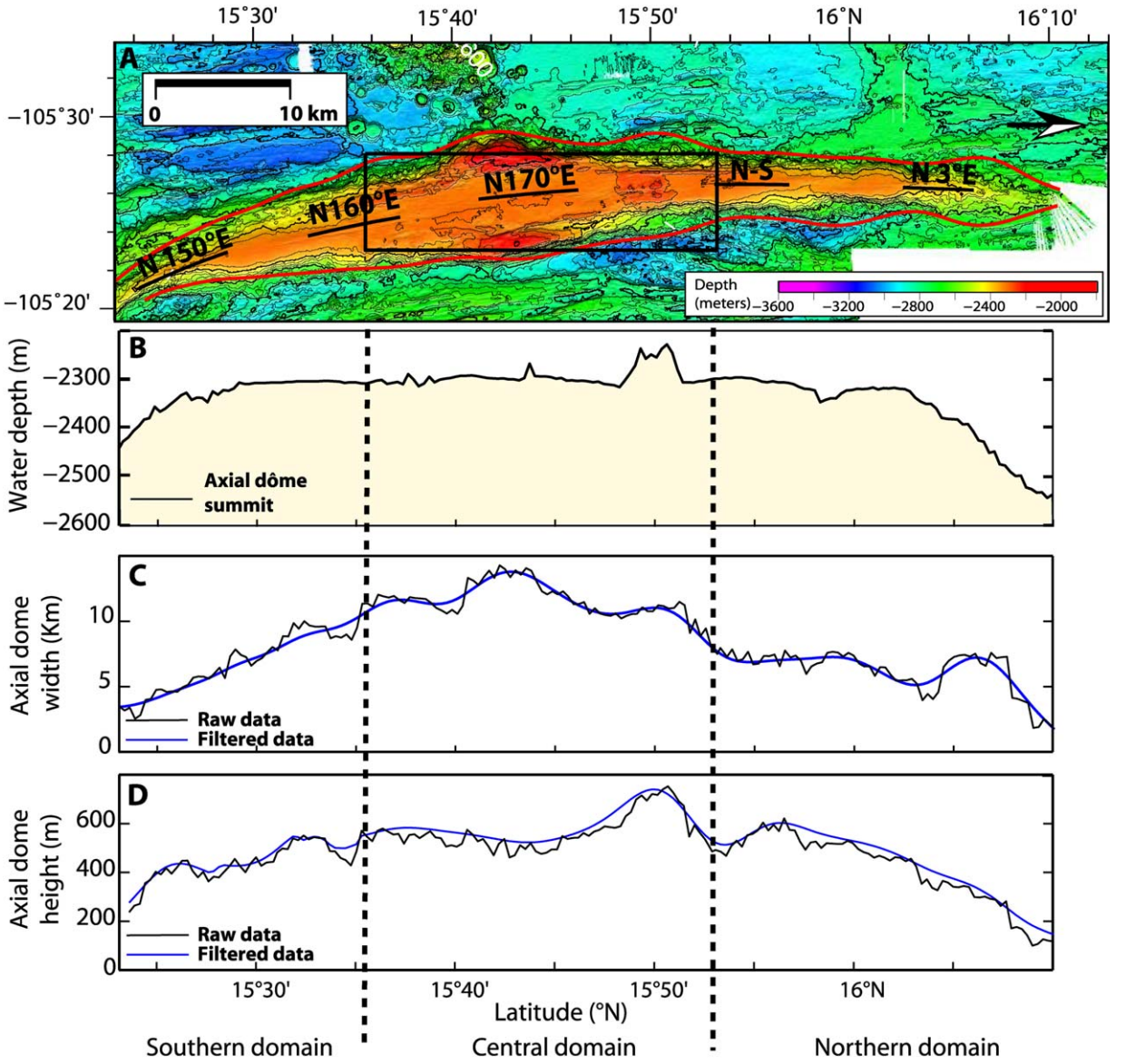


**Figure 3.** Axial morphology variations along the 16°N segment, calculated based on bathymetric profiles 16 km long and spaced 500 m apart, perpendicular to the axial dome. (a) Bathymetric map gridded with 40 m cells. The axial dome edges (red lines) are defined by the slope break between the relief of the axial dome and adjacent abyssal plains. The ridge axis trend is reported. The black box indicates the area where high-resolution bathymetry (1 m grid cell size) was collected using an Autonomous Underwater Vehicle (Figure 2); (b) Along-axis bathymetric profile; (c) Along-axis variation of the axial dome width. The limits of the three domains (south, central, and north) mentioned in the text are marked by dotted lines; (d) Along-axis variation of the height of the axial dome defined as the vertical distance between the base and the summit of the dome.

plains. Its width is less than 8 km and decreases toward the segment ends (Figure 3c). In these two domains, the Axial Summit Trough (AST) is clearly discerned based on the 40 m cells bathymetry. There is only one trough here, but it is not continuous, being made up of several successive segments in relay.

2. In the central domain, at the latitude of the Mathematician hotspot (~15°42'N), the axial dome, also displaying a "U" shape, is unusually wide and shallow (Figure 1), being 8–15 km wide at its base, and 500–780 m high above the adjacent abyssal plains (Figures 3c and 3d). Its summit consists in a subhorizontal (dipping less than 1°) and remarkably planar plateau bounded in the west and the east by large inward-facing normal faults which delimit 400 m high rims (Figure 1). According to *Carbotte et al.* [2000], these rims are relicts of an axial split seamount and correspond to regions where the layer 2A is particularly thick (550–750 m, see section 2.2). In this area, the AST is discontinuous, and, in some places, two subparallel AST are present.

The 1 m resolution bathymetric data collected between 15°36′N and 15°53′N (i.e., over 30 km along-axis) and covering the central part of the summit plateau (Figure 2a) allowed us to perform 5399 high-resolution bathymetric cross sections perpendicular to the ASTs. These profiles are 1200 m in length and 10 m apart. They are used to investigate in detail the along-axis variations of the geometry (depth, width) of the ASTs and of the depth of the summit plateau at their vicinity (Figure 4). At the axis, the floor depth varies between −2335 and −2230 m (Figure 4b). It deepens near 15°37′N, 15°48′N, and 15°51′N (by 35, 70, and 65 m, respectively), defining two long wavelength bulges in the topographic profile between 15°36′N and 15°53′N (Table 1). The three areas where the floor deepens correspond to discontinuities of the magma lens noted by *Carbotte et al*. [2000]: those at 15°48′N and 15°51′N correspond to disruptions of the reflector, the one at 15°37′N corresponds to a region where the reflector is poorly marked.

### 4.2. Along-Axis Variations of Axial Summit Trough Morphology

High-resolution bathymetry allows us to examine in detail the geometry of the Axial Summit Through (AST) over an area of 120 $km^2$ in the central part of the summit plateau (Figure 4). Here a Graben is considered to be an AST when we observe either similar and symmetric lava flows with opposed flow fronts on both sides, or divergent channels in the case of lobate lava flows.

In the central part of the summit plateau, the AST is divided into six segments (named segment A–F on Figure 4) 4–9.5 km in length, based on axis devals larger than 200 m or variations in the AST widths exceeding 150 m. These five major (third-order) discontinuities (noted D3 on Figure 4) are located near 15°37′N, 15°41′N, 15°45.5′N, 15°48′N, and 15°51′N (Table 1). As segments A and F are not fully covered by the high-resolution bathymetric data, their length is not taken into account in this study. Within these six segments, five additional minor (fourth-order) discontinuities are observed (noted D4 on Figure 4), characterized by slight (less than 200 m) lateral offsets of the ASTs. These five fourth-order discontinuities are located near 15°40.2′N, 15°42.8′N, 15°43.2′N, 15°44.8′N, and 15°52′N (Table 1).

The 10 discontinuities described above led us to define 12 1.1 to 9 km long AST segments numbered AST 1–AST 12 (Figures 2, 4, and Table 2). AST 1 and AST10 are only partially mapped by our data set, so that their lengths are not taken into account in the rest of the study.

Figure 4 indicates the variations of the morphology (width and depth) of these ASTs between 15°36′N and 15°53′N. They have various trends (N166°E–N175°E) that do not correlate with the overall orientation of the axial rise, the obliquity ranging between 2° and 10° (Figures 3a and 4) (see section 4.1). The ASTs are not systematically linear but are often slightly sinuous. As an example, the orientation of AST 12 varies by 4° when approaching a major discontinuity at 15°37′N.

The ASTs display significant variability in depth and width from one segment to the next. Their depth varies between 0.5 and 42 m with respect with the adjacent floor (Figure 4c and Table 2) but is generally less than 10 m. Their width varies from 8 to 1100 m (Figure 4d and Table 2), but generally remains below 150 m. When 1100 m wide, the AST is made up of an ensemble of straight and contiguous troughs that cannot be distinguished from each other (e.g., segment C).

Surprisingly, in some areas of the summit plateau, two contiguous ASTs coexist and overlap over distances of 800 m to 9 km. Over the 30 km of the surveyed axis, double ASTs are observed over a distance exceeding 20 km. The width of the two contiguous AST are sometimes comparable (ex. at 15°52′N, the two parallel AST are 70 and 100 m wide, respectively), but very often their width differs greatly, one being at least two to three times as wide as the other (ex. at latitude 15°38′N, the western AST is 150 m wide, while the eastern is 300 m wide, and at latitude 15°43′N, the western AST is 400 m wide and the eastern only 100 m).

### 4.3. Along-Axis Distribution of Volcanic Products

We have analyzed the distribution of the lava morphology in relation with the variation of the geometry of the axial dome and ASTs. Photographs and videos recorded during the Nautile dives were classified as: pillow lava, lobate lava, channels, collapsed lava lakes, and inflated lava. These observations were used as the basis for interpreting the lava facies throughout the high-resolution bathymetry (Figure 5). The facies were classified as "undifferentiated lava" where the bathymetric data lacked recognizable structures such as channels, lava lake pillars, pillow lava mounds etc., or where the seafloor was significantly disrupted by tectonic structures.

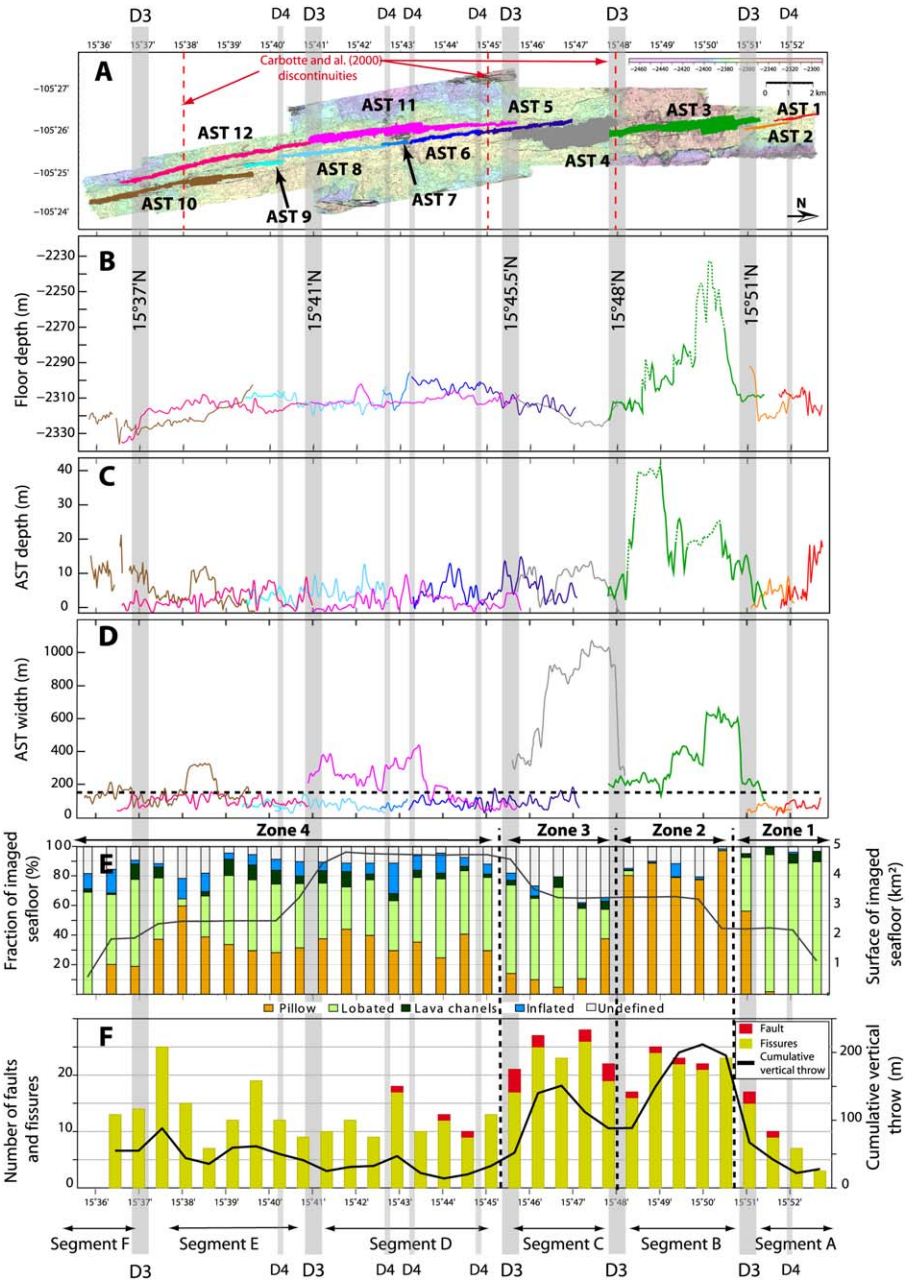


**Figure 4.** Along-axis variations of the Axial Summit Troughs (AST) morphologies, tectonic structures, and lava morphologies between 15°36′N and 15°53′N along the 16°N segment, East Pacific Rise. Third-order and fourth-order discontinuities (D3 and D4, respectively) defined in this study are reported in gray. (a) High-resolution bathymetric map (1 m grid cell size), with the location of AST 1–AST 12. The color code is the same for Figures 4a–4d and 2. The third-order discontinuities defined by *Carbotte et al*. [2000] based on side-scan sonar, are reported (red dashed vertical lines); (b) variation of the axial summit plateau depth in the vicinity of the ASTs, measured on transverse bathymetric cross-sections; (c) width of the ASTs measured based on transverse bathymetric cross-sections. The transition between a wide and a narrow AST is chosen at 150 m in this study (black dashed horizontal line); (d) depth of the ASTs measured; (e) proportion of seafloor occupied by each type of lava flow (pillow, lobate, inflated, lava channels, and undefined lava flows). Proportions are calculated based on the analysis of the abundance of each type of lava in the study area artificially divided into 1 km-wide strips perpendicular to the ASTs. The black line indicates the surface of seafloor imaged with high-resolution bathymetry; (f) along-axis variation of the abundance of faults and fissures, and cumulative vertical throw, calculated based on bathymetric profiles perpendicular to AST, and spaced 1 km apart.

Pillow lava usually extrudes in the form of individual bulbs or cylindrical tubes, which may be smooth or striated. Such lava often forms prominent mounds [e.g., *Moore*, 1975; *Embley and Chadwick*, 1994; *Perfit and Chadwick*, 1998].

**Table 1.** Characteristics of the Third and Fourth Discontinuities Between 15°36′N and 15°53′N, Based on This Study (Seafloor Deepening, Axial Summit Troughs (AST) Lateral Offsets, Changes in the AST Depth, Width, and Orientation, in the Abundance of Tectonic Features and in the Volcanic Facies Distribution) and on the Observations of *Carbotte et al.* [2000] (Magma Lens Disruption or Variation)

| | Discontinuities | Order 3 | Order 4 | Order 3 | Order 4 | Order 4 | Order 4 | Order 3 | Order 3 | Order 3 | Order 4 |
|---|---|---|---|---|---|---|---|---|---|---|---|
| This study[a] | Latitude | 15°37′N | 15°40.2′N | 15°41′N | 15°42.8′N | 15°43.2′N | 15°44.8′N | 15°45.5′N | 15°48′N | 15°51′N | 15°52′N |
| | Seafloor deepening (m) | 35 | No | No | No | No | No | No | 70 | 65 | no |
| | AST lateral offset (m) | 600 | 150 | 400 | 110 | 70 | 180 | 220 | 280 | 370 | 150 |
| | AST width variations (m) | 150 | 30 | 300 | 40 | 35 | 40 | 950 | 500 | 400 | 10 |
| | AST trend variations | 4° | 1° | 2° | 0 | 0 | 2° | 2° | 1° | 5° | 0 |
| | Volcanic facies variations | No | No | No | No | No | No | Yes | Yes | Yes | No |
| | Tectonic pattern variations | No | No | No | No | No | No | Yes | Yes | Yes | No |
| *Carbotte et al.* | Discontinuities latitude[b] | 15°38′N | - | - | - | - | - | 15°45′N | 15°48′N | - | - |
| [2000] | Magma lens[c] | Disruption | No | Disruption? | No | No | No | Depth variation | Disruption | Disruption | No |

[a]Based on high-resolution (1 m cells) bathymetry and bathymetric cross-sections, 1200 m long and 10 m spaced, perpendicular to Axial Summit Trough (AST).
[b]Based on side scan sonar SeaMarc II.
[c]Based on across and along axis seismic reflexion profiles.

Lobate lava are made up of long, flattened lobes laid down one by one (Figure 5). It is the equivalent of "Pahoehoe" lava on land. As they are laid down, their surface cools rapidly, forming a solid crust under which the molten lava continues to flow [e.g., *Hon et al.*, 1994; *Perfit and Chadwick*, 1998; *Soule et al.*, 2005; *Garry et al.*, 2006].

Channels and collapsed lava lakes, which are about 0.5–2 m deep, are typical features of lobate lava (Figure 5). When the level of lava decreases under the solidified crust as a result of drainage of lava toward lower zones or back into the dike, the crust can collapse, exposing the pillars that supported it. The floor of these collapse areas is generally made up of sheet or ropy lava flows [e.g., *Fink and Fletcher*, 1978; *Embley and Chadwick*, 1994].

Inflated lava flows have been described by *Deschamps et al.* [2014]. They form prominent flows, forming horizontal plateaus up to 700 m in diameter, with a flat or slightly depressed summit. Their edges consist of levees of 2–12 m, at the top of which fissures (inflation clefts) can be observed. These flows are made up of sheet and ropy lavas. They arise from the inflation of the Pahoehoe-type lava lobes emplaced on nearly flat seafloor [*Deschamps et al.*, 2014].

In the present study, the joint analysis of the direct observations by submersible and high-resolution bathymetry indicates a close association between the texture (rough, smooth), the seafloor morphology (monticules, hummocks), and the facies of a given lava. Based on these relationships, a geological map (Figure 2b) is drawn for the whole zone covered by the high-resolution bathymetric data. This allows the statistical analysis of the abundance of each type of lava, by dividing the study area into 32, 1 km wide strips perpendicular to the AST. For each cell defined in this way, the area occupied by each type of lava is calculated and

**Table 2.** Geometrical Characteristics of Axial Summit Troughs (AST)[a]

| AST Number | AST Length (m) | AST Orientation | AST Depth (m) | AST Width (m) | Narrow (<150 m) AST | Wide (>150 m) AST | % of Length Where the AST Overlaps With Another One | Number of the Adjacent AST |
|---|---|---|---|---|---|---|---|---|
| 1 | 1900 | N170°E | 1–19 | 13–125 | X | | 35% | 2 |
| 2 | 1450 | N170°E | 0.5–12 | 22–111 | X | | 70% | 1; 3 |
| 3 | 6500 | N175°E | 0.5–42 | 39–689 | | X | 17% | 2; 4 |
| 4 | 4330 | N174°E | 0.5–15 | 280–1100 | | X | 68% | 3; 5 |
| 5 | 4500 | N172°E | 0.5–19 | 13–199 | X | | 100% | 4; 11 |
| 6 | 3020 | N172°E | 1–18 | 24–158 | X | | 100% | 11 |
| 7 | 1150 | N172°E | 2.5–14 | 30–112 | X | | 100% | 11 |
| 8 | 4670 | N174°E | 0.5–15 | 17–151 | X | | 100% | 11 |
| 9 | 1680 | N173°E | 1–9 | 39–118 | X | | 100% | 12 |
| 10 | 7100 | N170°E | 0.5–21 | 66–333 | | X | 77% | 12 |
| 11 | 8910 | N171°E | 0.5–13 | 8–464 | | between 15°44′N and 15°41′N | 100% | 5; 6; 7; 8 |
| 12 | 9080 | N166°E–N169°E | 0.5–12 | 20–195 | X | | 100% | 9; 10 |

[a]Orientation, depth, and width are measured based on bathymetric cross sections, 1200 m long and 10 m spaced, perpendicular to AST. The transition between a wide and a narrow AST is set here at 150 m.

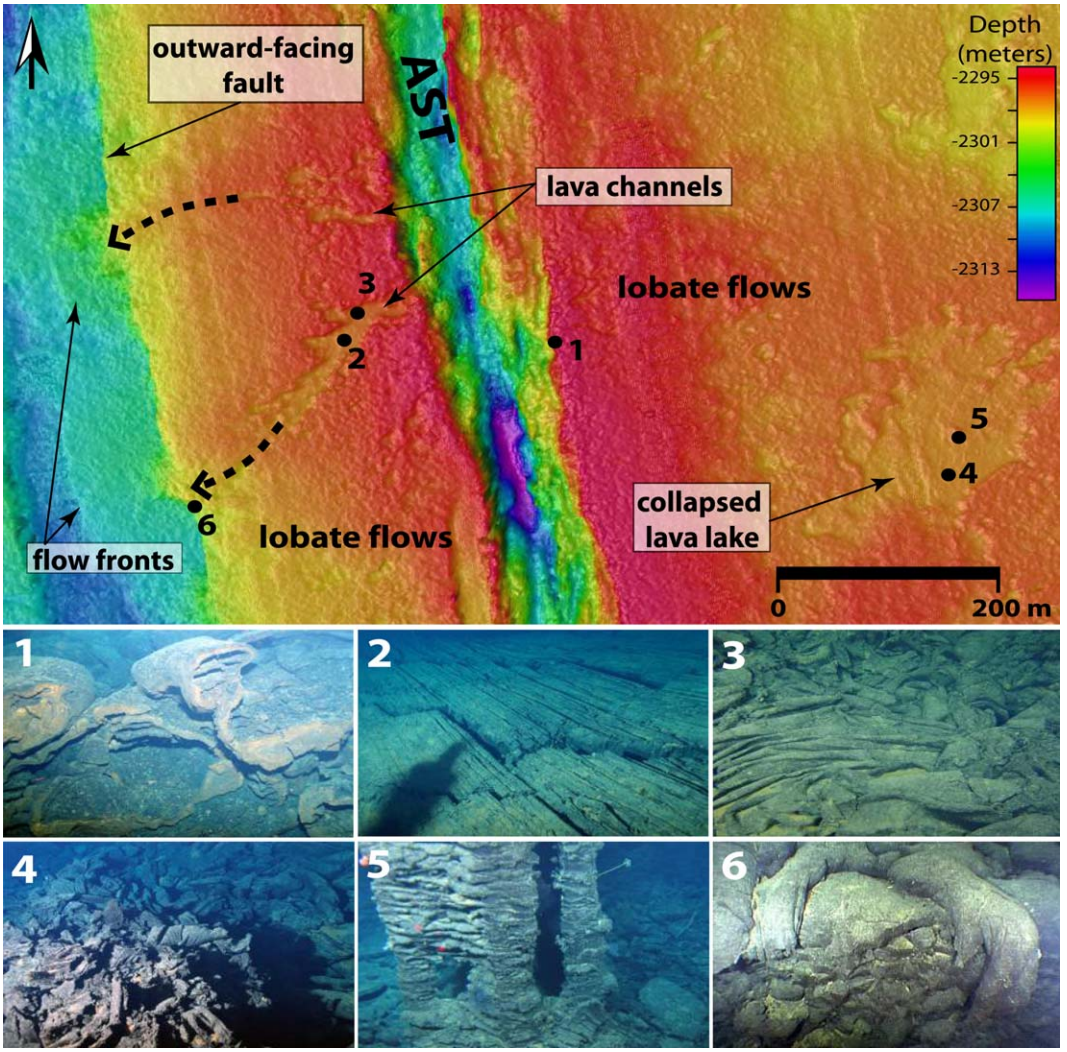


**Figure 5.** High-resolution bathymetry (1 m grid cell size) blowout showing lava channels and collapsed lava lakes within lobate lava flows. The dashed arrows indicate lava flowing over an outward-facing fault scarp. Photos were acquired with submersible Nautile dives during PARISUB cruise in 2010. Location is indicated on Figure 2.

normalized to percent of total (Figure 4e). We find that the volcanic facies are not uniformly distributed along the axis in the study area. Four zones are discriminated based on their distribution (Figure 4e):

1. From 15°36′N to 15°45.5′N (zone 4), the seafloor is characterized by an abundance of lobate lavas (57%, of which 5% are channels) generally observed close to the AST. The pillow lava (32%) are mostly located toward the edges of the summit plateau. The rest of the zone is made up of inflated lava (8%) and undifferentiated lava (3%).
2. Between 15°45.5′N and 15°48′N (zone 3), the terrain is also mostly covered with lobate lavas (55%, of which 4% are channels) but with a higher amount of "undifferentiated lava" (33%) due to the great abundance of tectonic structures that partly obliterate lava facies. Pillow flows cover 18% of this zone, and inflated flows 4%.
3. Between 15°48′N and 15°51′N (zone 2), the terrain is mostly composed of pillow lava (81%), which forms a prominent edifice ~6 km in diameter and 80 m high with respect to the surrounding seafloor, composed of agglomerated mounds 100–500 m in diameter each. At its summit, some smooth-surfaced inflated lava are seen (3%).
4. Between 15°51′N and 15°53′N (zone 1), the terrain mainly consists of lobate lava (97%, of which 6% are channels). The rest is made up of inflated lava (1%) and undifferentiated lava (2%).

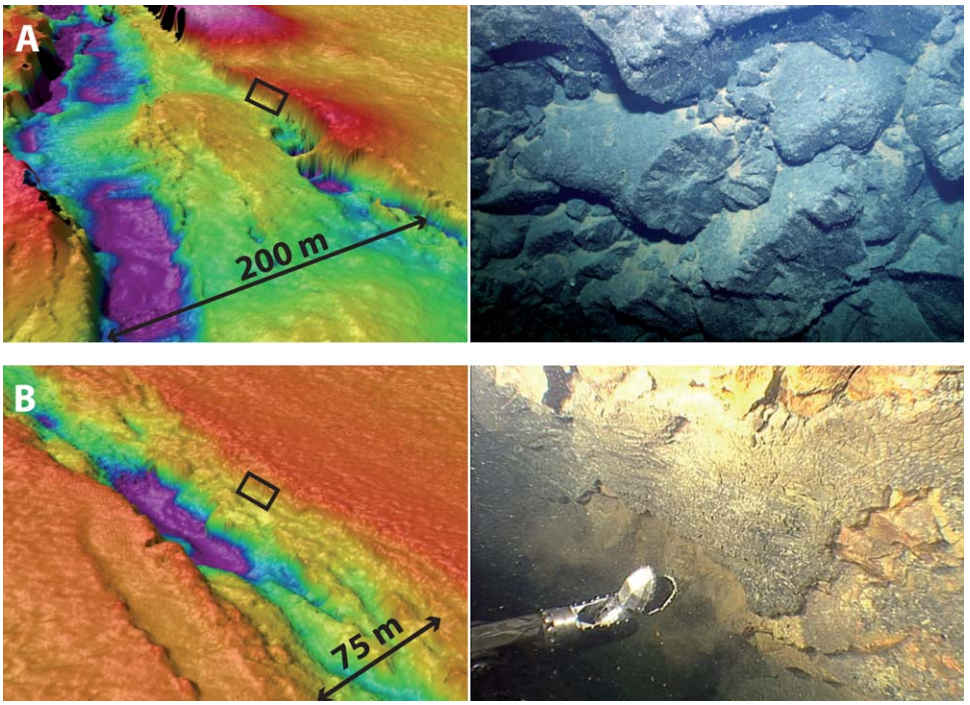


**Figure 6.** 3-D views (location on Figure 2) and photos (located by black rectangles) of a narrow (< 150 m –wide) and a large (> 150 m) Axial Summit Trough (AST), showing the morphology of its bounding faults. (a) Border of a wide AST. The steep (> 70°) and sharp-edged fault exposes former pristine lava sections and is. not covered by subsequent volcanic flows; (b) border of a narrow AST partially covered by lava deposits. The AST wall consequently displays a jagged shape, and nonuniform, moderate dips (< 55°). On the photo, the fault plane displays horizontal selvages reflecting the different lava lake levels during drainage. Photos acquired by the submersible Nautile during the PARISUB cruise (2010).

The boundaries of the four zones discriminated based on the distribution of the different types of lava, correspond to the third-order discontinuities observed by *Carbotte et al.* [2000] at 15°45.5′N, 15°48′N, and 15°51′N based on the interruptions in the magma lens, while being slightly offset (by up to 900 m, in the case of the discontinuities located near 15°45′N). They sometimes also correspond to abrupt variations in the width of the AST (at 15°45.5′N, for example) (section 4.2), or to areas where the summit plateau deepens (15°48′N and 15°51′N, for example) (section 4.1) (Table 1).

### 4.4. Along-Axis Distribution of Tectonic Structures

Here we analyze the distribution of faults and fissures along the axis in relation with the volcanic flows and edifices, the axial dome and the ASTs geometries. In the center of each 1 km wide cells defined in section 4.3, an east-west bathymetric section was made to analyze statistically the abundance of tectonic structures and measure their dip and vertical throw. The statistical analysis of faults and fissures does not take into account the large (up to 70 m high) and likely much older faults that bound the summit plateau rims. Depending on the bathymetric section considered, 3–26 faults and 0–4 fissures per section are reported (Figure 4f). The apparent dip of the faults ranges from 14° to 88°, and their vertical throw from 0.5 to 45 m. The cumulative vertical throw along each bathymetric profile ranges from 14 to 212 m.

The four zones that have been discriminated based on volcanic facies (section 4.3) display contrasted tectonic patterns (Figures 4e and 4f). Faults and fissures are more abundant in zones 2 and 3, with 23 faults per profile on average, compared with 10 faults per profile in zones 1 and 4. They also have larger cumulative vertical throws (up to 150 versus 50 m at maximum in zones 1 and 4). In zones 1 and 4, the AST-bounding faults display relatively low dips (45° in average) and vertical offsets (5 and 7 m in average, respectively). In zone 2, faults that cut across the prominent, 6 km in diameter, pillow edifice, display the steepest dips (> 65°), and the most elevated vertical throws (up to 45 m) of the segment. It is worth noting that in this area, the AST-bounding faults trend N173°N, i.e., slightly oblique to the overall orientation of the AST 3 (N175°E). Zone 3 is the region where the AST is the widest (∼1100 m) and made up of a set of contiguous and parallel narrow grabens and fissures. In this area, the AST fault-bounding scarps are also slightly oblique (N171°E) to

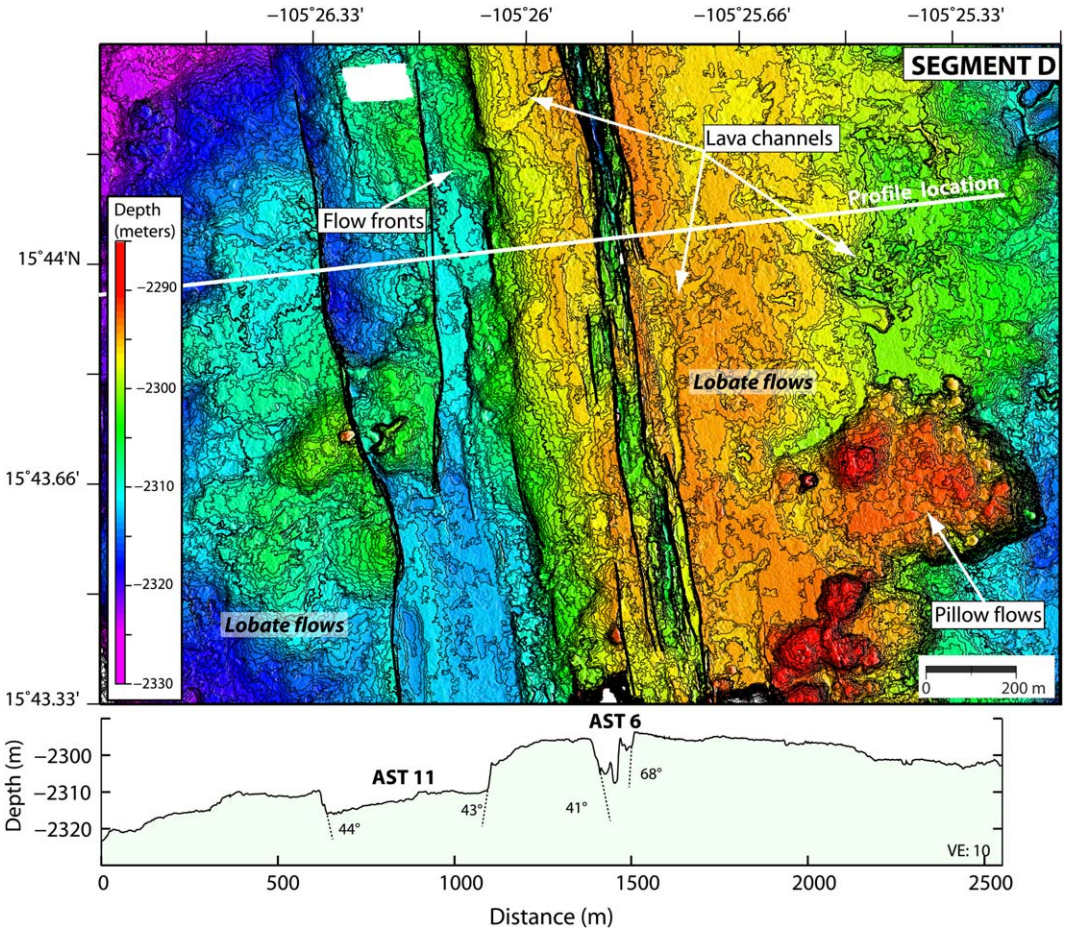


**Figure 7.** Detailed high-resolution (1 m grid cell size) bathymetry (see location on Figure 2) showing parallel Axial Summit Troughs AST 6 and AST 11 in the segment. The main lava flows morphologies and fault associated with ASTs (bold lines) are indicated. Lobate lava flows originating from AST 6 (which is centered on the axial dome) are transported both sides of the AST through lava channels. In the west, flows are clearly cut by the AST 11, which is itself partially filled with more recent lobate lava emitted from the eastern AST 6. The bathymetric profile highlights the differences in the geometry of the two contiguous ASTs.

the general trend of the AST 4 (N174°E). Their vertical throws (9 m in average) and their dips (50° to 70°) are lower than in zone 2.

The along-axis distribution of the deformation thus highlights four contrasted domains that coincide with those identified based on the lava morphology (Table 1). Their edges locate at 15°45.5′N, 15°48′N, and 15°51′N, thus coinciding with the third-order discontinuities of the AST evidenced based on high-resolution bathymetry (see section 4.2). Consequently, zone 1 corresponds to segment A, zone 2 to segment B, zone 3 to segment C. However, no significant variation in the volcanic and tectonic patterns is observed within zone 4 although it contains third-order discontinuities defining segments D, E, and F.

### 4.5. Relations Between the Axial Summit Troughs and Lava Emission

When the AST is wide ($>$ 150 m) (AST 3 and AST 4 in segments B and C for example), there is no evidence of any recent volcanic activity, either based on the high-resolution bathymetric data or videos. The AST fault-bounding planes have steep dips ($>$ 50°) and expose pristine lava sections, which they obviously postdate (Figure 6a).

When the AST is narrow ($<$ 150 m) (AST 1 and AST 2 in segment A, AST 10 in segment F for example), lava flows partially mask the AST bounding faults, which display jagged shapes and irregular and generally lower dips ($<$ 50°), thus clearly postdating fault activity (Figure 6b).

As indicated in section 4.2, two contiguous and nearly parallel ASTs are often observed. In this case, their volcanic activity is contrasted. As an example, for segment D, the eastern AST (made up of ASTs 6, 7, and 8

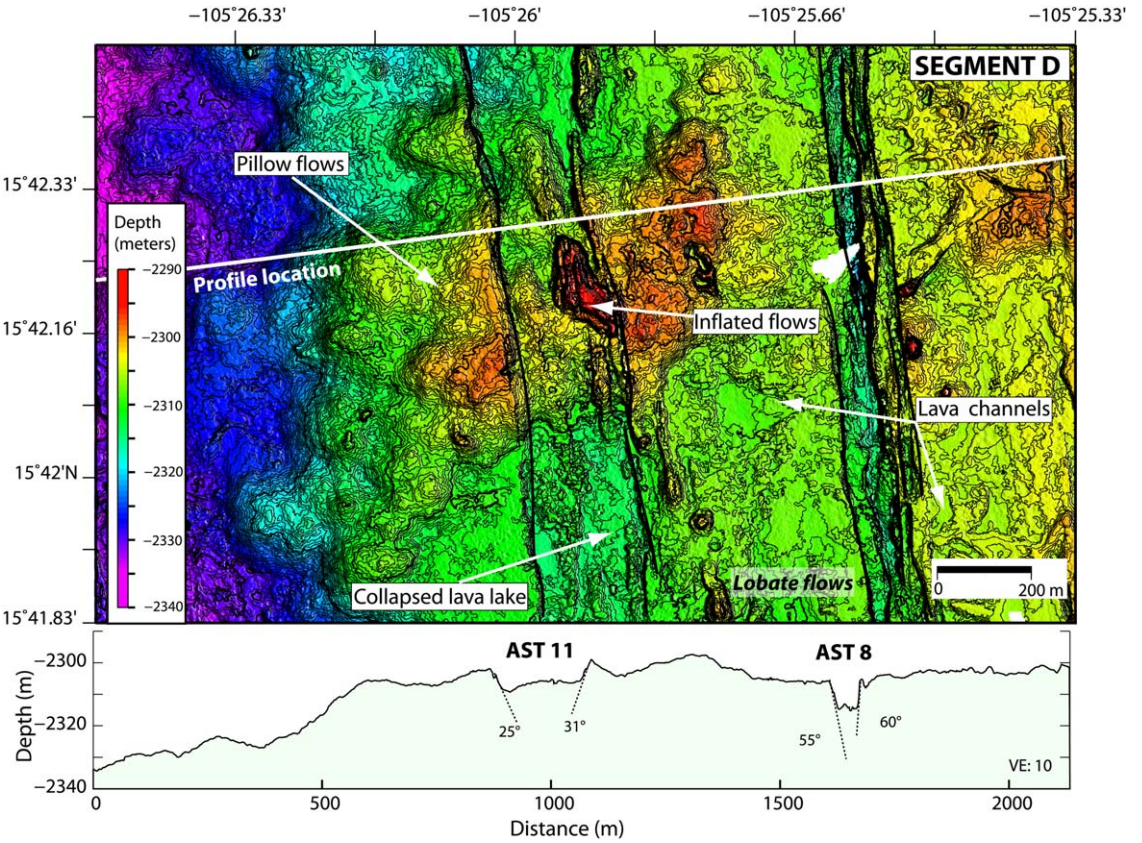


**Figure 8.** Detailed high-resolution (1 m grid cell size) bathymetry (see location on Figure 2) showing the Axial Summit Troughs AST 8 and AST 11 within segment D. The main lava flows morphologies and main faults (in bold lines) are indicated. Recent pillow mounds and inflated flows within the westernmost AST 11 indicate that it has been recently the source of eruptions. Lava channels on both sides of the eastern AST 8 indicate that it has also been the source of eruptions. The bathymetric profile highlights the differences in the geometry of the two contiguous AST.

(Figure 4a)), which is the narrowest, produced a great amount of lobate lava flows transported by channels on both sides (Figure 7). The western AST (AST 11) has also been a source of eruptions, building a pillow lava mound, 1 km in diameter, with inflated lava at its summit (Figure 8). Flows originating from the eastern ASTs are clearly cut by the western one, which has been itself partially filled with more recent lobate lava from the eastern AST (Figures 5 and 7). The volcanic activity of both the eastern and western ASTs was thus clearly synchronous, at least recently, which is consistent with the existence of a magma lens under both of them [*Carbotte et al*., 2000]. The eastern AST, which is centered on the axial dome, has produced a greater volume of lava and has been the source of the most recent eruptions. Segment E also displays two contiguous ASTs. The western one (AST 12), which is the narrowest (up to 130 m wide), has produced recent pillow and inflated lava (Figure 9). Some of these inflated flows are located within the AST and partially mask it bounding faults. The eastern AST (AST 10) is wider (400 m) and deeper (by 10 m) than the western AST 12, and it has not been the site of recent eruptions (Figure 9). Its bounding faults are indeed large (vertical throws up to 25 m), sharp edged, and display steep dips (up to 75°). The AST 10 continues southward onto segment F where it becomes single and narrow (less than 150 m in width) and locates at the summit of the axial dome as AST 12 progressively disappears. Traces of recent eruptions (pillow and inflated lava) can be seen there.

## 5. Discussion

### 5.1. Fine-Scale Segmentation of the Ridge Axis at 16°N

Previous studies have shown that fast-spreading ridges are segmented on several scales (10–1000 km). First and second-order discontinuities are defined either by transform faults by propagating rifts. They delimit segments 50–1000 km long that are laterally shifted by more than 3 km. They have lifespans of at least 0.5 million years [e.g., *Macdonald*, 2001].

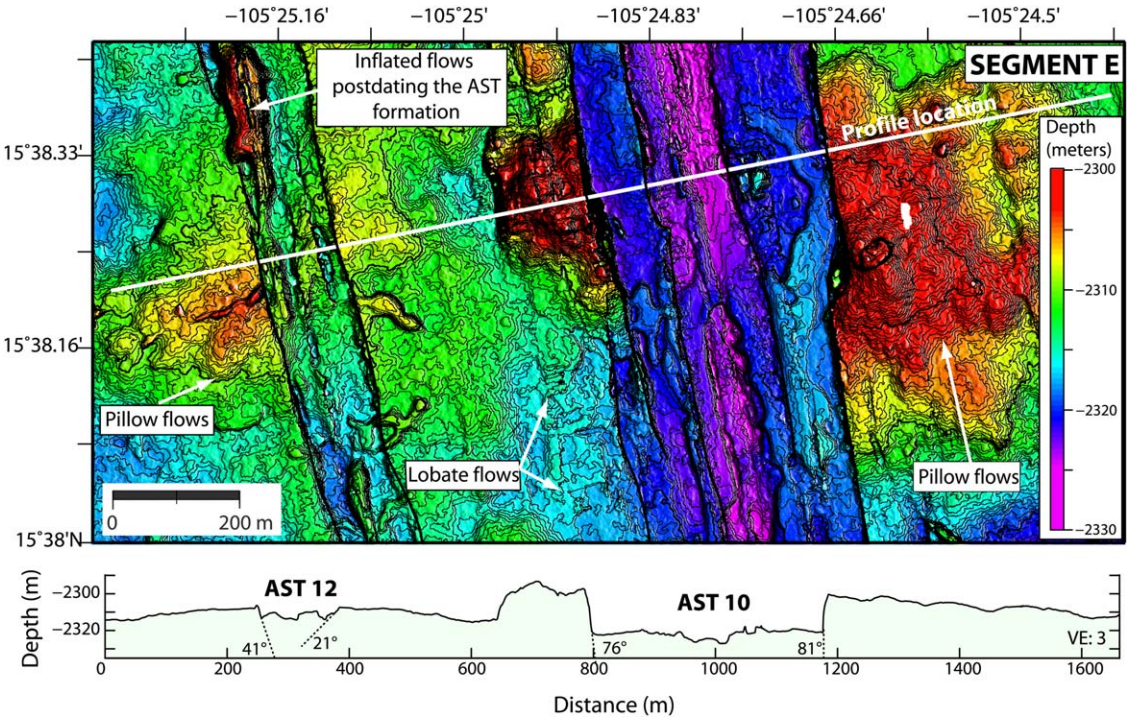


**Figure 9.** Detailed high-resolution (1 m grid cell size) bathymetry (see location on Figure 2) showing the Axial Summit Troughs AST 10 and AST 12 in segment E. The main lava flows morphologies and faults are indicated. The AST 12 (the narrowest of segment E), centered on a volcanic ridge, has produced pillow and inflated lava recently. No trace of recent eruption is observed within the Eastern AST 10, the widest one at this location. The bathymetric profile highlights the differences in the geometry of the two contiguous AST.

Third-order discontinuities delimit segments 20 ± 10 km long. They correspond to axis devals ranging from 200 m to 3 km, and/or to a deepening of the axial seafloor by more than 20 m [e.g., *Macdonald et al*., 1984, 1988, 1991; *Haymon and White*, 2004]. This third-order segmentation is thought to be linked to magma input, which often is reduced at the extremities of a segment relative to its center. Consistently, on other regions of the EPR (18°30′S–17°15′S and 9°08′N–10°N for example), lavas reflecting a high effusion rate or low viscosity (e.g. lobate, ropy, and sheet lava) are observed in the center of the third-order segments, and lavas reflecting a low effusion rate or high viscosity (e.g. pillow lava) are ubiquitous at their extremities [e.g., *White et al*., 2000, 2002]. These observations are corroborated by seismic reflection data, which indicate a correlation between the geometry of the magma lens and the third-order segmentation: at the end of a segment, the lens is deeper and narrower leading to less intense volcanic activity in terms of volume or effusion rate [e.g., *Detrick et al*., 1987; *Sinton and Detrick*, 1992; *Kent et al*., 1993; *Toomey et al*., 1994; *White et al*., 2002]. Third-order segments commonly have lifespans between 10,000 and 100,000 years [*Haymon and White*, 2004].

Between 15°36′N and 15°53′N, the axis is segmented into six, 4–9.5 km long, segments (segments A–F, Figure 4) bounded by five major (third-order) discontinuities. Segment A is located in zone 1, B in zone 2, C in zone 3, and segments D, E, F in zone 4 (see sections 4.3 and 4.4). These five discontinuities are located at 15°37′N, 15°41′N, 15°45.5′N, 15°48′N, and 15°51′N. They correspond either to lateral offsets (by 200–600 m) or to abrupt variations of the geometry (width and depth) or trend (by up to 5°) of the ASTs (Table 1). In some cases, they coincide with significant seafloor deepening (35–70 m). These discontinuities also often mark the apparition or disappearance of ASTs, such that the six segments herein defined display either a single (AST 3 in segment B for example) or two contiguous ASTs (AST 6,7, 8, and 11 in segment D).

Three of the large discontinuities we mapped (15°37′N, 15°45.5′N, and 15°48′N) correspond to third-order discontinuities observed by *Carbotte et al*. [2000] based on side-scan sonar data but their position is here slightly refined (Table 1 and Figure 4). Four of them (15°37′N, 15°45.5′N, 15°48′N, and 15°51′N) coincide either with interruption or complete disappearance of the magma lens, or variation of its depth [*Carbotte et al*., 2000] (Table 1). The relative abundance of the different lava facies is in some cases of the same order in two contiguous segments. As an example, segment D and E, both located in zone 4, display 41% and

36% of lobate flows, 35% and 37% of pillow flows and 9% of inflated lava flows, respectively (see section 4.3; Figure 4). Conversely, between other contiguous segments, the lava morphology can be contrasted. For example, lobate lava largely dominate (> 97%) in segment A, while pillow lava dominate (> 80%) on the segment B (see section 4.3) (Figure 4). These contrasts in lava morphology from one segment to another reflect different eruptive styles, either in relation with the effusion rate itself depending on the magma viscosity (thus temperature, composition, gas content), on the dike width, and on the magma chamber internal pressure that gradually decreases during eruption [*Gregg and Fink*, 1995; *Griffiths*, 2000]. Contrasted eruptive styles from one segment to another could also be related here to distinct sources, which would be consistent with the presence of several magma lens with variable width and depths [*Carbotte et al*., 2000]. As the slope in the vicinity of ATSs is nearly constant along axis (with values ranging 0.5–1.5°), it probably does not control here the lava morphology.

The above mentioned variations in ASTs morphology, tectonic pattern, and eruptive style from one segment to another, as well as the presence of well-marked discontinuities between them confirm that these six 4–9.5 km long segments are third-order segments according to the classifications proposed by *Macdonald et al*. [1984, 1988], *Haymon et al*. [1991], *White et al*. [2000], and *Haymon and White* [2004]. Their position is refined here based on our high-resolution data (Table 1).

Within these six third-order segments, we observe five more subtle discontinuities spaced 1–4 km apart, (named "D4" on Figure 4) that disrupt and laterally shift the AST, near 15°40.2'N, 15°42.8'N, 15°43.2'N, 15°44.8'N, and 15°52'N. Twelve ASTs (named AST 1–AST 12) can herein be defined (Figures 2 and 4). These discontinuities were not reported in previous studies of the 16°N EPR segment. Indeed, the devals between the ASTs have an amplitude ranging only between 70 and 200 m, and these discontinuities do not correlate to any significant deepening or AST trend change, nor variation of the geometry of the magma lens, nor variations in lava morphology and tectonic patterns. These discontinuities are therefore typically fourth-order discontinuities according to the classifications by previous authors: fourth-order discontinuities indeed typically delimit segments 7 ± 5 km long [e.g., *Haymon and White*, 2004]. They correspond to lateral axis devals less than 200 m [e.g., *Macdonald et al*., 1984, 1988; *Haymon et al*., 1991; *White et al*., 2000, 2002]. This segmentation is unstable, it could be directly associated with single episodes of dike intrusion into the upper crust. Fourth-order discontinuities are defined as boundaries of areas subjected to deformation due to swarms of fissures and grabens resulting from dike intrusions which did not all lead to a surface eruption [e.g., *Haymon et al*., 1991, 1993; *Wright et al*., 1995; *Cormier et al*., 2003; *Haymon and White*, 2004]. In contrast to third-order discontinuities, they do not correspond to variations in the deep structure of the segment or to the geometry of the underlying magma chamber. This explains why there is no variation in eruptive style along fourth-order segments and why they have a lifespan of under 1000 years, linked to the frequency of intrusive events [*Haymon and White*, 2004].

### 5.2. Magmatic Processes Along the Axial Summit Trough

#### 5.2.1. Previous Models of Axial Summit Trough Evolution

On most of the segments of the EPR, an Axial Summit Trough (AST) runs along the summit of the axial dome [e.g., *Kappel and Ryan*, 1986; *Gente et al*., 1986; *Fornari et al*., 1998; *Carbotte et al*., 2006]. These ASTs are generally 5–10 m in depth and about 40 m wide, but they are sometimes deeper (up to 50 m) and wider (up to 400 m). Sometimes, no AST is observed at all [e.g., *Chadwick and Embley*, 1998; *Soule et al*., 2009]. It is agreed that the AST is formed in response to dike intrusions [e.g., *Rubin and Pollard*, 1988; *Mastin and Pollard*, 1988; *Rubin*, 1992; *Chadwick and Embley*, 1998; *Cormier et al*., 2003; *Carbotte et al*., 2006; *Soule et al*., 2009]. Indeed, numerical [*Rubin and Pollard*, 1988; *Rubin*, 1992] and analog models [*Mastin and Pollard*, 1988] show that the stresses caused by a dike intrusion are accommodated on the surface by the formation of sets of fissures and grabens. These models were confirmed by geodetic observations and measurements in emerged rift zones [e.g., *Rubin*, 1992; *Chadwick and Embley*, 1998]. A well-documented example is an intrusion at the Krafla volcano (North Iceland) in 1977, where the intrusion of a dike, revealed by of the propagation of a seismic swarm, has led to the formation of normal faults and the deposition of lava a couple of hours later [*Larsen et al*., 1979].

The evolution of ASTs through time remains a subject of debate. Many authors suggest a cyclic evolution, with the AST broadening and deepening during tectonic phases alternating with magmatic ones. Other

studies propose a more continuous (or "stationary") evolution via dike intrusion events spaced evenly in time.

*Kappel and Ryan* [1986] and *Gente et al*. [1986] propose a model of cyclic evolution, for the Juan de Fuca intermediate—spreading ridge and the fast—spreading EPR (13°N). Initially, during a period of intense magmatic activity, an axial dome without any summit trough would form due to successive eruptions (phases T1, T2). As the magma input decreases, a trough would initiate and progressively broaden at the dome summit (phase T3). During a gradual return of magmatic activity, the trough would continue to widen by tectonic extension, but the traces of this activity would be masked by lava flows erupted from axial eruptive fissures (phase T4). These successive eruptions would lead to the formation of a new axial dome. Phases T1 and T2 are therefore considered as "magmatic" phases, and T3 and T4 as "tectonic" phases. This model is similar to the one proposed by *Cormier et al*. [2003] on the EPR (17°S) and *Deschamps et al*. [2013] for the intermediate-spreading Explorer ridge.

Other similar but more detailed models have been proposed for the segment 9°N of the EPR. [*Fornari et al*., 1998; *Soule et al*., 2009]. *Fornari et al*. [1998] propose that a narrow and shallow trough (width and depth below 200 and 15 m, respectively) forms by collapse within the lobate lava flows above the fissures induced by subsurface dikes. These collapses would result from lava drain back into the feeding dike at the end of the eruption. They suggest that the trough forms during a period of intense magmatic activity, as its edges are not normal faults as shown by their scalloped shape. The trough would be indeed too narrow to be bounded by fault planes and the brittle crust at the axis too thin to sustain shear failure. The trough would widen (300–3000 m) and deepen (30–100 m) by extension along bounding faults during phases of starved magmatic activity. Conversely *Soule et al*. [2009] suggest that during periods of intense volcanic, narrow (less than 100 m -wide) ASTs formed by subsidence related to a dike intrusion are already edged with fault planes but that are often partially overprinted by volcanic deposits. A decrease of the volcanic activity, but with continued diking events without systematic eruption onto the seafloor, would also lead to a widening (150–300 m) and deepening (8–20 m) of the AST.

In contrast, *Carbotte et al*. [2006] propose a "steady-state" accretion model for the Juan de Fuca ridge. Their analysis of the AST dimensions with regard to crustal magma bodies indicates that the width and depth of the trough diminish where the magma body disappears, rather than deepening and widening, as expected for rift topography due to tectonic extension. These authors propose that the AST initially forms directly above dikes, and broadens as the result of repeated dike intrusions, the deformation being localized along the AST-bounding faults, and the volcanic products issued from these eruptions remaining confined within the AST.

#### 5.2.2. Magmatic Processes Along the 16°N Segment Revealed by AST Geometry

We have shown above how the ATS morphology can greatly vary from one third-order segment to another (Figure 4). Here we analyze how the AST geometry relates to the volcanic activity.

In the case of a narrow ($<$ 150 m) and shallow ($<$ 10 m) AST, it is located at the summit of the axial dome, above a shallow magma lens ($\sim$1.3 km below the seafloor), and shows evidence for recent volcanic eruptions (Figures 7–9). It is bounded by fault planes with moderate dips (less than 55°) and vertical throws (less than 8 m), often partially masked by volcanic flows. These are either inflated lava flows or relicts of lava lakes that have filled the AST before lava drain back. AST filling followed by drain back would explain its scalloped edges and the horizontal selvages onto its walls, reflecting successive lava levels during drainage.

Where the AST is wide ($>$ 150 m) and deep ($>$ 10 m), tectonic features are more abundant, and their dips and vertical throws greater ($>$ 50° and 8 m, respectively) and they often clearly post date the most recent lava flows, exposing pristine lava sections (Figure 6a).

The variations of the AST width and depth do not correlate with changes of the depth of the magma lens and of the top of the layer 2B, which suggests that AST morphology variations do not reflect major changes in the balance between tectonic and magmatic processes at the time scale of the third-order segmentation (i.e. thousands of years). As an example, the magma lens has a constant depth of about 1.4 km below segments C and D, that are characterized by wide ($\sim$1100 m) and narrow ($\sim$100 m) ASTs, respectively. We therefore hypothesize that AST widening reflects a decrease in eruptive volcanic activity but with continued dike intrusions at the origin of abundant sets of fissures and faults that are not masked by volcanic deposits.

Narrow AST bounded by scalloped and more subdued walls would reflect a period of higher volcanic activity. Our observations do not support the model of *Carbotte et al*. [2000] who suggest that narrow ASTs correspond to decreased magmatic activity related to a deep magma chamber and that wide ASTs develop as a response to successive and frequent dike intrusions above a shallower magma chamber.

When two contiguous and parallel ASTs run along a segment and when one AST is larger than the other, our study indicates the narrowest one is indeed more volcanically active than the widest one. For example, along segment D, the activity of all the ASTs has been clearly synchronous (see section 4.5), at least recently, which is in agreement with the observation of a magma lens below all of them [*Carbotte et al*., 2000]. The eastern trough, the narrowest, has emitted a greater volume of lava building an axial volcanic ridge and is presently be the most volcanically active of the two (Figure 7). Along segment E, traces of the most recent volcanic activity are identified at the western trough (the narrowest of the two), which also marks the summit of the axial volcanic ridge.

Contiguous ASTs behave as relay zones, the narrower one being systematically volcanically more active and lengthening at the expense of the wider one. For example, at segment D, the narrow eastern trough (AST 6, 7, 8) appears to propagate southward at the expense of the wide western trough (AST 11). South of the third-order discontinuity located at ∼15°41′N, AST 11 evolves into the narrow AST12, which itself propagates southward at the expense of AST 10 (segment E). Such segment instabilities are likely related the nearby hotspot, and likely reflect short-term variations (i.e. hundreds of years to a thousand years). Such a zone of warmer mantle likely triggers enhanced mantle melting and a greater magma flux under the spreading ridge. This is corroborated by the bull's eye gravity low centered on the highest and widest zone of the dome near 15°42′N, which indicates an overthickened crust or a hotter mantle associated with a larger melting zone [*Weiland and Macdonald*, 1996; *Shah and Buck*, 2006]. As a result, segments tend to propagate away from the hotspot latitude, the "hot" and most volcanically active segments lengthening at the expense of neighboring "colder" segments [e.g., *Thibaud et al*., 1998].

It is worth noting that despite of the bow shape of the axial dome toward the west as its trend varies by 33° from north to south, the orientation of the ASTs does not vary significantly along-axis (less than 9°). The greater number of third and fourth-order discontinuities with respect to other fast-spreading segments results from the general bow shape of the (second-order) segment. For example, the same number of discontinuities (i.e., five third-order and five fourth-order discontinuities) are identified over a distance of 90 km at the 9°N segment of the EPR [*Haymon and White*, 2004] but only over 30 km the case of the 16°N segment, based on data with similar (∼1 m) resolutions. In the case of the 16°N segment, the third and fourth-order segments are arranged *en echelon*, forming a global V-shape centered near latitude ∼15°42′N, where the axial rise is the broadest, thus accommodating the axial dome curvature. This pattern is likely due to the influence of the hotspot located to the west. Its proximity is indeed likely responsible for the presence of the two magma lens observed by *Carbotte et al*. [2000], the main one being up to 1600 m wide and centered below the ASTs, and the second one being deeper (by ∼300 m) and located under the western half of the axial summit plateau, at a distance of at least 1.2 km west of the dome axis. As a result, the diking zone is particularly wide (1100 m minimum) and the diking events are poorly localized between latitudes 15°37′N and 15°48′N.

## 6. Conclusions

Our study has described the segmentation of the Axial Summit Trough (AST) along the 16°N segment between 15°36′N and 15°53′N. Based on the high-resolution bathymetry and videos, we have evidenced two new third-order discontinuities, and also confirmed and refined the location of three ones that have been previously identified [*Macdonald et al*., 1992; *Carbotte et al*., 2000]. These discontinuities are revealed by lateral offsets (larger than 200 m) of the AST, changes in the AST depth, width and trend, and by variations in the abundance of tectonic features and in the volcanic facies. They correspond to magma lens disruption and depth variation, confirming that they reflect along-axis variation in the magma plumbing system. They bound six 4–9.5 km long third-order spreading segments, themselves subdivided by five fourth-order discontinuities. These more subtle discontinuities correspond to AST disruption or devals of 70–200 m in amplitude. No significant volcanic or tectonic pattern, nor magma lens variation occur along these fourth-order segments, confirming that they relate to few (perhaps even individual) diking events, as suggested by previous authors [e.g., *Haymon and White*, 2004].

The morphology of the 12 ASTs defined by third and fourth-order discontinuities dramatically varies along-axis. Narrow (< 150 m in width) and shallow (< 10 m) ASTs are located at the summit of axial volcanic ridges. They have been the source of the most recent volcanic eruptions, being fully or partially filled by lava flows that sometimes have drained back, leaving horizontal selvages reflecting successive lava lake levels during drainage, and irregular and more subdued AST bounding faults obscured by lava flows. However, they are not solely formed by the collapse of lava flows directly above dike intrusions as suggested by *Fornari et al*. [1998], since movements on the fault planes alongside them are involved in their development. These narrow AST reflect-enhanced volcanic activity compared to the wider and deeper ASTs, which display a greater amount of linear and well-defined faults, fissures and grabens. We thus hypothesize that AST widening and deepening reflects a decrease in the number of dikes reaching the seafloor to produce eruptions covering the tectonic features. They would thus indicate a declining volcanic activity on the seafloor but with continued dike intrusions in depth at the origin fissures, faults, and graben at the surface, as proposed by *Soule et al*. [2009] for the 9°N segment of the EPR. This would explain why the magma lens does not deepen or disappear beneath wide ASTs (such as AST 4 along segment C for example) and why volcanic activity is almost synchronous along contiguous narrow and wide ASTs. Our results thus do not corroborate the models of cyclic ridge evolution implying alternating tectonic and magmatic phases [e.g., *Kappel and Ryan*, 1986] nor the models of steady-state evolution that suggest the AST deepens and widens during periods of enhanced magmatic activity [e.g., *Carbotte et al*., 2006].

The existence of two parallel and contiguous ASTs over a distance of about 20 km and above a wide (∼1600 m) magma lens, indicates a wide (1100 m minimum) zone of diking and thus the poor localization of the magmatic processes likely in relation with the nearby Mathematician hotspot. The global "en echelon" shift of the ASTs to progressively accommodate the bow shape of the axial dome in the direction of the hotspot, the propagation of several ASTs away from the hotspot latitude, and the existence of a second, deeper, magma lens under the western half of the axial summit plateau, support this hypothesis. The presence of the hotspot at less than 20 km of the ridge axis likely induces an instability of the accretionary processes due to the presence a warmer mantle that causes enhanced mantle melting in the vicinity of 15°42'N, i.e., where the axial dome is the broadest and displays two contiguous AST.

To conclude, the Mathematician hotspot influences the spreading processes along the 16°N segment at the scale of few tens meters (i.e., minor lateral offsets of the AST at fourth-order discontinuities) up to 100 km (i.e., the bow shape of the 115 km long axial dome). As a consequence, the AST is characterized by greater variations in its geometry (width, depth, orientation, linearity) and is segmented at a shorter wavelength than those of the other segments of the EPR, the greater number of third and fourth-order discontinuities with respect to other fast-spreading segments directly resulting from the general bow shape of the segment.

**Acknowledgments**
We thank the crew of the R/V l'Atalante, the engineers, and technicians from Genavir and the PARISUB scientific teams. We would like to thank the Woods Hole Oceanographic Institution where this work initiated. This work was supported by a PhD Scholarship of Brittany Region and Université de Bretagne Occidentale (France) and has benefited from funding by the Europôle Mer and Labex-Mer of the European Institute for Marine Studies (IUEM). The high-resolution bathymetric data are available upon request through the NAUTILUS (the French national oceanographic data center) portal (http://www.ifremer.fr/sismer/).

## References

Carbotte, S. M., C. Mutter, J. C. Mutter, and G. Ponce-Correa (1998), Influence of magma supply and spreading rate on crustal magma bodies and emplacement of the extrusive layer: Insights from the East Pacific Rise at lat 16 degrees N, *Geology*, *26*(5), 455–458, doi:10.1130/0091-7613.

Carbotte, S. M., A. Solomon, and G. Ponce-Correa (2000), Evaluation of morphological indicators of magma supply and segmentation from a seismic reflection study of the East Pacific Rise 15°30′–17°N, *J. Geophys. Res.*, *105*(B2), 2737–2759, doi:10.1029/1999JB900245.

Carbotte, S. M., R. S. Detrick, A. Harding, J. P. Canales, J. Babcock, G. Kent, E. Van Ark, M. R. Nedimovic, and J. Diebold (2006), Rift topography linked to magmatism at the intermediate spreading Juan de Fuca Ridge, *Geology*, *34*(3), 209–212, doi:10.1130/G21969.1.

Carlut, J., M.-H. Cormier, D. V. Kent, K. E. Donnelly, and C. H. Langmuir (2004), Timing of volcanism along the northern East Pacific Rise based on paleointensity experiments on basaltic glasses, *J. Geophys. Res.*, *109*(B4), 1978–2012, doi:10.1029/2003JB002672.

Chadwick, W. W., and R. W. Embley (1998), Graben formation associated with recent dike intrusions and volcanic eruptions on the mid-ocean ridge, *J. Geophys. Res.*, *103*(B5), 9807–9825, doi:10.1029/97JB02485.

Cormier, M.-H., K. C. Macdonald, and D. S. Wilson (1995), A three-dimensional gravity analysis of the East Pacific Rise from 18 degrees to 21 degrees 30'S, *J. Geophys. Res.*, *100*(B5), 8063–8082, doi:10.1029/95JB00243.

Cormier, M.-H., W. B. F. Ryan, A. K. Shah, W. Jin, A. M. Bradley, and D. R. Yoerger (2003), Waxing and waning volcanism along the East Pacific Rise on a millennium time scale, *Geology*, *31*(7), 633–636, doi:10.1130/0091-7613.

Deschamps, A., M. A. Tivey, W. W. Chadwick, and R. W. Embley (2013), Waning magmatic activity along the Southern Explorer Ridge revealed through fault restoration of rift topography, *Geochem. Geophys. Geosystems*, *14*, 1609–1625, doi:10.1002/ggge.20110.

Deschamps, A., C. Grigné, M. Le Saout, S. A. Soule, P. Allemand, B. Van Vliet-Lanoe, and F. Floc'h (2014), Morphology and dynamics of inflated subaqueous basaltic lava flows, *Geochem. Geophys. Geosystems*, *15*, 2128–2150, doi:10.1002/2014GC005274.

Detrick, R. S., P. Buhl, E. Vera, J. Mutter, J. Orcutt, J. Madsen, and T. Brocher (1987), Multi-channel seismic imaging of a crustal magma chamber along the East Pacific Rise, *Nature*, *326*(6108), 35–41, doi:10.1038/326035a0.

Embley, R. W., and W. W. Chadwick (1994), Volcanic and hydrothermal processes associated with a recent phase of seafloor spreading at the northern Cleft Segment: Juan de Fuca Ridge, *J. Geophys. Res.*, *99*(B3), 4741–4760, doi:10.1029/93JB02038.

Fink, J. H., and R. C. Fletcher (1978), Ropy pahoehoe: Surface folding of a viscous fluid, *J. Volcanol. Geotherm. Res.*, *4*(1-2), 151–170.
Fornari, D. J., R. M. Haymon, M. R. Perfit, T. K. P. Gregg, and M. H. Edwards (1998), Axial summit trough of the East Pacific Rise 9 degrees −10 degrees N: Geological characteristics and evolution of the axial zone on fast spreading mid-ocean ridges, *J. Geophys. Res.*, *103*(B5), 9827–9855, doi:10.1029/98JB00028.
Garry, W. B., T. K. P. Gregg, S. A. Soule, and D. J. Fornari (2006), Formation of submarine lava channel textures: Insights from laboratory simulations, *J. Geophys. Res.*, *111*, B03104, doi:10.1029/2005JB003796.
Gente, P., J. M. Auzende, V. Renard, Y. Fouquet, and D. Bideau (1986), Detailed geological mapping by submersible of the East Pacific Rise axial Graben near 13°N, *Earth Planet. Sci. Lett.*, *78*(2–3), 224–236, doi:10.1016/0012-821X(86)90063-4.
Gregg, T. K. P., and J. H. Fink (1995), Quantification of submarine lava-flow morphology through analog experiments, *Geology*, *23*(1), 73–76, doi:10.1130/0091-7613.
Griffiths, R. W. (2000), The dynamics of lava flows, *Annu. Rev. Fluid Mech.*, *32*(1), 477–518.
Haymon, R. M., D. J. Fornari, M. H. Edwards, S. M. Carbotte, D. Wright, and K. C. MacDonald (1991), Hydrothermal vent distribution along the East Pacific Rise crest (9 degrees 09′-54′N) and its relationship to magmatic and tectonic processes on fast-spreading mid-ocean ridges, *Earth Planet. Sci. Lett.*, *104*(2-4), 513–534.
Haymon, R. M. et al. (1993), Volcanic eruption of the mid-ocean ridge along the East Pacific Rise crest at 9 degrees 45–52′N: Direct submersible observations of seafloor phenomena associated with an eruption event in April, 1991, *Earth Planet. Sci. Lett.*, *119*(1-2), 85–101.
Hey, R. (1977), Tectonic evolution of the Cocos-Nazca spreading center, *Geol. Soc. Am. Bull.*, *88*(10), 1404–1420.
Hon, K., J. Kauahikaua, R. Denlinger, and K. Mackay (1994), Emplacement and inflation of pahoehoe sheet flows: Observations and measurements of active lava flows on Kilauea Volcano, Hawaii, *Geol. Soc. Am. Bull.*, *106*(3), 351–370, doi:10.1130/0016-7606.
Ito, G., J. Lin, and D. Graham (2003), Observational and theoretical studies of the dynamics of mantle plume–mid-ocean ridge interaction, *Rev. Geophys.*, *41*(4), 1017, doi:10.1029/2002RG000117.
Kappel, E. S., and W. B. F. Ryan (1986), Volcanic episodicity and a non-steady state rift valley along Northeast Pacific spreading centers: Evidence from Sea MARC I, *J. Geophys. Res.*, *91*(B14), 13,925–13,940, doi:10.1029/JB091iB14p13925.
Kent, G. M., A. J. Harding, and J. A. Orcutt (1990), Evidence for a smaller magma chamber beneath the East Pacific Rise at 9°30′ N, *Nature*, *344*(6267), 650–653, doi:10.1038/344650a0.
Kent, G. M., A. J. Harding, and J. A. Orcutt (1993), Distribution of magma beneath the East Pacific Rise between the Clipperton Transform and the 9 degrees 17′N Deval from forward modeling of common depth point data, *J. Geophys. Res.*, *98*(B8), 13,945–13,969, doi:10.1029/93JB00705.
Kent, G. M., A. J. Harding, J. A. Orcutt, R. S. Detrick, J. C. Mutter, and P. Buhl (1994), Uniform accretion of oceanic crust south of the Garrett transform at 14°15′S on the East Pacific Rise, *J. Geophys. Res.*, *99*(B5), 9097–9116, doi:10.1029/93JB02872.
Larsen, G., K. Groenvold, and S. Thorarinsson (1979), Volcanic eruption through a geothermal borehole at Namafjall, Iceland, *Nature*, *278*(5706), 707–710.
Macdonald, K. C. (2001), Mid-ocean ridge tectonics, volcanism and geomorphology, in *Encyclopedia of Ocean Sciences*, edited by John H. Steele, pp. 1798–1813, Academic, Oxford, U. K.
Macdonald, K. C., J.-C. Sempere, and P. J. Fox (1984), East Pacific Rise from Siqueiros to Orozco fracture zones: Along-strike continuity of axial neovolcanic zone and structure and evolution of overlapping spreading centers, *J. Geophys. Res.*, *89*(B7), 6049–6069, doi:10.1029/JB089iB07p06049.
Macdonald, K. C., P. J. Fox, L. J. Perram, M. F. Eisen, R. M. Haymon, S. P. Miller, S. M. Carbotte, M. H. Cormier, and A. N. Shor (1988), A new view of the mid-ocean ridge from the behaviour of ridge-axis discontinuities, *Nature*, *335*(6187), 217–225.
Macdonald, K. C., D. S. Scheirer, and S. M. Carbotte (1991), Mid-ocean ridges: Discontinuities, segments and giant cracks, *Science*, *253*(5023), 986–994.
Macdonald, K. C., P. J. Fox, S. Miller, S. Carbotte, M. H. Edwards, M. Eisen, D. J. Fornari, L. Perram, R. Pockalny, and D. Scheirer (1992), The East Pacific Rise and its flanks 8–18 N: History of segmentation, propagation and spreading direction based on SeaMARC II and Sea Beam studies, *Mar. Geophys. Res.*, *14*(4), 299–344.
Maia, M. et al. (2000), The Pacific-Antarctic Ridge-Foundation Hotspot interaction: A case study of a ridge approaching a hotspot, *Mar. Geol.*, *167*(1-2), 61–84.
Mammerickx, J., and D. Sandwell (1986), Rifting of old oceanic lithosphere, *J. Geophys. Res.*, *91*(B2), 1975–1988, doi:10.1029/JB091iB02p01975.
Mastin, L. G., and D. D. Pollard (1988), Surface deformation and shallow dike intrusion processes at Inyo Craters, Long Valley, California, *J. Geophys. Res.*, *93*(B11), 13,221–13,235, doi:10.1029/JB093iB11p13221.
Mittelstaedt, E., G. Ito, and M. D. Behn (2008), Mid-ocean ridge jumps associated with hotspot magmatism, *Earth Planet. Sci. Lett.*, *266*(3-4), 256–270, doi:10.1016/j.epsl.2007.10.055.
Mittelstaedt, E., G. Ito, and J. van Hunen (2011), Repeat ridge jumps associated with plume-ridge interaction, melt transport, and ridge migration, *J. Geophys. Res.*, *116*, B01102, doi:10.1029/2010JB007504.
Moore, J. G. (1975), Mechanism of formation of pillow lava, *Am. Sci.*, *63*(3), 269–277.
Mougel, B., A. Agranier, C. Hemond, and P. Gente (2014), A highly unradiogenic lead isotopic signature revealed by volcanic rocks from the East Pacific Rise, *Nat. Commun.*, *5*, 4474, doi:10.1038/ncomms5474.
Perfit, M. R., and W. W. Chadwick (1998), Magmatism at mid-ocean ridges: Constraints from volcanological and geochemical investigations, *Geophys. Monogr.*, *106*, 59–115.
Rubin, A. M. (1992), Dike-induced faulting and Graben subsidence in volcanic rift zones, *J. Geophys. Res.*, *97*(B2), 1839–1858, doi:10.1029/91JB02170.
Rubin, A. M., and D. D. Pollard (1988), Dike-induced faulting in rift zones of Iceland and Afar, *Geology*, *16*(5), 413–417, doi:10.1130/0091-7613.
Scheirer, D. S., and K. C. Macdonald (1993), Variation in cross-sectional area of the axial ridge along the East Pacific Rise: Evidence for the magmatic budget of a fast spreading center, *J. Geophys. Res.*, *98*(B5), 7871–7885, doi:10.1029/93JB00015.
Scheirer, D. S., and K. C. Macdonald (1995), Near-axis seamounts on the flanks of the East Pacific Rise, 8 degrees N to 17 degrees N, *J. Geophys. Res.*, *100*(B2), 2239–2259, doi:10.1029/94JB02769.
Sempere, J.-C., and K. C. Macdonald (1986), Overlapping spreading centers: Implications from crack growth simulation by the displacement discontinuity method, *Tectonics*, *5*(1), 151–163, doi:10.1029/TC005i001p00151.
Shah, A. K., and W. R. Buck (2006), The rise and fall of axial highs during ridge jumps, *J. Geophys. Res.*, *111* B08101, doi:10.1029/2005JB003657.

Sinton, J., R. Detrick, J. P. Canales, G. Ito, and M. Behn (2003), Morphology and segmentation of the western Galápagos Spreading Center, 90.5°–98°W: Plume-ridge interaction at an intermediate spreading ridge, *Geochem. Geophys. Geosystems*, *4*(12), 8515, doi:10.1029/2003GC000609.

Sinton, J. M., and R. S. Detrick (1992), Mid-ocean ridge magma chambers, *J. Geophys. Res.*, *97*(B1), 197–216, doi:10.1029/91JB02508.

Sloan, H. (1991), Temporal evolution of overlapping spreading centers at 16 degrees 20'N on the East Pacific Rise, *Mar. Geol.*, *97*(3-4), 315–324.

Soule, S. A., D. J. Fornari, M. R. Perfit, M. A. Tivey, W. I. Ridley, and H. Schouten (2005), Channelized lava flows at the East Pacific Rise crest, 9 degrees −10 degrees N: The importance of off-axis lava transport in developing the architecture of young oceanic crust, *Geochem. Geophys. Geosystems*, *6*, Q08005, doi:10.1029/2005GC000912.

Soule, S. A., J. Escartin, and D. J. Fornari (2009), A record of eruption and intrusion at a fast spreading ridge axis: Axial summit trough of the East Pacific Rise at 9–10 degrees N, *Geochem. Geophys. Geosystems*, *10*, Q10T07, doi:10.1029/2008GC002354.

Thibaud, R., P. Gente, and M. Maia (1998), A systematic analysis of the Mid-Atlantic Ridge morphology and gravity between 15 degrees N and 40 degrees N: Constraints of the thermal structure, *J. Geophys. Res.*, *103*(B10), 24, doi:10.1029/97JB02934.

Toomey, D. R., S. C. Solomon, and G. M. Purdy (1994), Tomographic imaging of the shallow crustal structure of the East Pacific Rise at 9 degrees 30'N, *J. Geophys. Res.*, *99*(B12), 24,135–24,157, doi:10.1029/94JB01942.

Wang, X., J. R. Cochran, and G. A. Barth (1996), Gravity anomalies, crustal thickness, and the pattern of mantle flow at the fast spreading East Pacific Rise, 9 degrees −10 degrees N: Evidence for three-dimensional upwelling, *J. Geophys. Res.*, *101*(B8), 17,927–17,940, doi:10.1029/96JB00194.

Weiland, C. M., and K. C. Macdonald (1996), Geophysical study of the East Pacific Rise 15 degrees N-17 degrees N: An unusually robust segment, *J. Geophys. Res.*, *101*(B9), 20,257–20273, doi:10.1029/96JB01756.

White, S. M., K. C. Macdonald, and R. M. Haymon (2000), Basaltic lava domes, lava lakes, and volcanic segmentation on the southern East Pacific Rise, *J. Geophys. Res.*, *105*(B10), 23,519–23,536, doi:10.1029/2000JB900248.

White, S. M., R. M. Haymon, D. J. Fornari, M. R. Perfit, and K. C. Macdonald (2002), Correlation between volcanic and tectonic segmentation of fast-spreading ridges: Evidence from volcanic structures and laval flow morphology on the East Pacific Rise at 9 degrees −10 degrees N, *J. Geophys. Res.*, *107*(B8), doi:10.1029/2001JB000571.

Wright, D. J., R. M. Haymon, and D. J. Fornari (1995), Crustal fissuring and its relationship to magmatic and hydrothermal processes on the East Pacific Rise crest (9 degrees 12' to 54'N), *J. Geophys. Res.*, *100*(B4), 6097–6120, doi:10.1029/94JB02876.